The effects of the spatial distribution of bottom topography and bottom drag on seiche-induced wave train formation

Anton Baglaenko, Marek Stastna, Derek T. Steinmoeller and Francis J. Poulin

ABSTRACT

We consider the nonlinear, non-hydrostatic dynamics of seiches in small to medium-sized lakes. Using numerical simulations of shallow water equations modified to include weakly non-hydrostatic effects, we illustrate how spatially varying bottom drag and finite amplitude topography lead to the bending of wave trains that develop from the initial standing wave. For the case of variable topography, we discuss how the seiche and the wave trains that develop can resuspend material (e.g. nutrients) from the bottom of the lake and redistribute it in space. The numerical methods employed are spectrally accurate in space and second-order in time, yielding excellent accuracy and little numerical dissipation. We find that while the resuspension itself is largely due to the long standing waves at early times, the redistribution of nutrient distribution that is seen at later times is profoundly influenced by the development of the wave trains; a fundamentally non-hydrostatic effect.

Key words | bathymetry, bottom drag, fluid dynamics, numerical simulations, nutrient redistribution

Anton Baglaenko (corresponding author)
Marek Stastna
Derek T. Steinmoeller
Francis J. Poulin
Department of Applied Mathematics,
University of Waterloo,
200 University Ave,
Waterloo,
Ontario,
Canada N2 L 3G1
E-mail: *abaglaen@uwaterloo.ca*

INTRODUCTION

Lakes, through their part in the hydrological cycle, their modification of local climate and weather, and the habitat they provide for life forms ranging over invertebrates, fish, birds and mammals, are essential to a functioning biosphere. Lakes provide humanity with a source of freshwater, food and a focus for agricultural activities in their surroundings. Studying the physical behaviour of lakes and the various biogeochemical cycles contained within is important for both theoretical and observational science. The purpose of this article is to consider a fundamental, nonlinear process that is typically induced by sustained winds over the lake: the breakdown of a seiche (or standing wave) into a nonlinear and non-hydrostatic wave train. While this process is well known to occur in the field (Hodges *et al.* 2000; Boegman *et al.* 2003), we aim to explore how the process is modified by the presence of localized regions of high bottom drag and topography using numerical simulations.

Our long-term goal is to understand the entire range of motions from lake-scale to small-scale turbulent flows, herein we focus on motions that are predominantly horizontal. The effects of bottom boundary layer turbulence are thus parameterized in the commonly used quadratic bottom drag law. Similarly, the effects of finite amplitude topography are included, but wave breaking and the resulting turbulence are not. The model employed is simpler than lake-scale models such as the Estuary, Lake and Coastal Ocean Model (ELCOM) (Hodges *et al.* 2000) and the MIT General Circulation Model (MIT GCM) (Marshall *et al.* 2012), but has the advantage of representing nonlinear, non-hydrostatic processes in a compact, numerically tractable manner that is suitable for exploring theoretical questions. Moreover, simple models like the one we use do not require strong horizontal eddy viscosity and diffusivity to maintain stability, and thus allow for the construction of numerical schemes that have a minimal amount of numerical dissipation.

doi: 10.2166/wqrjc.2012.005

This approach is somewhat different from past literature. As an example, Hodges *et al.* (2000) compare ELCOM results to thermistor chain measurements for Lake Kinneret, Israel. These simulations have a great deal of practical significance since Kinneret is an important source of freshwater. Moreover, this lake has a very simple geometry. This implies that measurements of basin-scale internal waves are possible to carry out with a reasonable number of measuring stations. A second Lake Kinneret study by Boegman *et al.* (2003) discusses field measurements demonstrating that internal waves degenerate from basin-scale into high-frequency waves. Both of these papers use between six and 10 measurement sites to extrapolate to basin-scale features. While the results of Hodges *et al.* (2000) are important, the numerical model they use is hydrostatic, making the simulation of high-frequency, non-hydrostatic waves impossible.

While lake and ocean models come in a range of complexity and a variety of numerical methodologies, no present model can resolve motions from the lake scale down to boundary layer processes. The issue of expressing friction and drag, specifically when dealing with bottom boundary layer effects is thus a critical one. We have chosen to employ a long-accepted model for the study of stratified lake motion (Fischer *et al.* 1979). The idea is to separate the lake into vertical layers, which provides a reasonable approximation of basin-scale internal wave effects. The classical way to drive such a model is to allow for wind to impart energy to the system through the top layer and to allow this motion to drive flow (via pressure and possibly shear stress) in the lower layers (see Imberger (1998) and Wuest & Lorke (2003) for a discussion of energy propagation and de la Fuente *et al.* (2008) for a similarly layered numerical model). In order to study the effects of bottom drag and nonlinear friction, we follow a similar theoretical framework, focusing on the effect of bottom drag in a single layer system. The results would naturally extend to a multi-layer model with the drag in the bottom layer.

Damping

The bottom drag we have chosen to study takes the form $C_D|\boldsymbol{u}|\boldsymbol{u}h$, where $\boldsymbol{u}$ denotes the velocity, and h the layer depth. The dimensions of C_D are m^{-1} and the corresponding dimensionless coefficient is written as c_D. C_D is nondimensionalized by the turbulent boundary layer depth, H_b (Arbic & Scott 2008), a parameter that has no single universal value and may vary in space. Nevertheless, the quadratic law is a common way of expressing drag in many forms, from the classical problem of a vertically thrown ball in a fluid (Timmerman & van der Weele 1999), to various expressions of bottom roughness with a varying drag parameter (e.g. Ullman & Wilson (1998), who relate c_D experimentally to the root mean square bottom roughness). Most lake models use a constant value of c_D or vary it as a model parameter (Longuet-Higgins (1970) and Ozkan-Haller & Kirby (1999) use values of c_D to fit model predictions to observed lake behaviour). More complete literature surveys can be found in Fredsoe & Deigaard (1992) and Van Rijn (1994). The results of Arbic & Scott (2008) for geostrophic turbulence suggest that fairly substantial variations of c_D yield similar behaviour. For our own investigations, we will use an accepted value of $c_D = 0.0025$, and vary the value in certain numerical experiments in order to demonstrate the system's sensitivity to this parameter.

Quadratic drag is commonly used when attempting to describe flow in comparatively shallow, rough regions such as the continental shelf: Koblinsky (1981) examines quadratic drag in the West Florida shelf with a value of $c_D = 0.002$; Bowers *et al.* (1991) examine the effect of drag on incoming M_2 and S_2 tidal waves and argue for situationally increased values of c_D based on bottom roughness and topography, but find values generally very close to the accepted value to be sufficient; Feddersen *et al.* (2003) consider variations of the drag coefficient in the nearshore based on bottom roughness and topography. Over coral reefs (Kunkel *et al.* 2006; Fernando *et al.* 2008) extremely high values of $c_D = 0.05$ have been employed.

It is important to remember that although commonly used, quadratic drag is an ad hoc parameterization of drag and friction. Hasselmann *et al.* (1980), in a large experimental survey of tides in the North Sea, found that the quadratic bottom drag law is not a good approximation of the dynamics of shallow water coastal regions. Similarly, Pingree (1983), analysing quadratic friction and tides, numerically argues that the quadratic drag law is not a valid approximation of the energy drain in the

system. Alternatively, Godin & Martnez (1994) examine the effects of quadratic drag with the accepted coefficient in tidal channels and determine that this drag parameterization yields qualitatively correct behaviour. From these discussions it is clear that quadratic damping has components which are qualitatively correct (as its use has been empirically verified) but requires further research in order to fully understand the regimes in which it is appropriate.

Topography

Secondly, we present an investigation of how bottom topography alters the seiche breakdown process, and in turn affects the resuspension of sediment (and hence nutrients) into the main water column in analogy with work by Hearn *et al.* (2001) on nutrient uptake from coral reefs. In many boreal lakes, the majority of the lake is nutrient poor (i.e. the lake is oligotrophic). Thus, in oligotrophic lakes, nutrient distribution is by far the limiting factor on plankton and algae growth, and sediment resuspension has the potential to enrich the main water column with profound influence on the lake ecosystem.

The effects of bottom topography are investigated through numerical simulations using the same weakly non-hydrostatic shallow water model used for bottom damping experiment simulations. The numerical experiments are performed for several configurations of bottom topography in order to further our understanding of the effects of specific orientation of the bottom topography on pick up and redistribution. The pick up scheme used is an ad hoc parameterization which is motivated by empirical observations, but is kept as simple as possible.

The numerical method used throughout is based on a Fourier pseudospectral method with leapfrog time-stepping. In the so-called pseudospectral method, derivatives are computed in spectral space, i.e. the space of the Fourier expansion coefficients (obtained with FFT), and products are performed in physical space (see Boyd (2001)). An exponential wave number cut-off filter is employed in spectral space after each time-step to prevent aliasing errors and numerical instabilities. Even and odd continuations are employed to impose no flux boundary conditions at the lake edge.

Numerical experiments performed as part of the model validation indicate that third order Adams-Bashforth (AB) required a time-step roughly one-seventh of that used with leapfrog to maintain stability (see Durran (1991) for a comparison of AB and leapfrog numerical schemes). Thus while high order time-stepping could be introduced into the model, the small typical values of time-step ensure that the leapfrog method employed yields highly accurate results. The quadratic bottom drag is easy to implement as part of the explicit step.

Aliasing due to the nonlinear terms is controlled by the use of either spectral filtering with an exponentially decaying filter ranging from one to zero over all wave numbers larger than two-thirds of the largest resolved wave number, or fourth order hyperviscosity (see Boyd (2001) for a discussion of the pros and cons of these alternatives). The choice of filter was not found to influence the simulations on the timescales shown. All simulations were confirmed to be grid independent via grid halving and doubling sensitivity tests, and we thus conclude that the results of the simulations are robust. The pseudospectral method used here has very little inherent numerical dissipation, and this allows us to focus on the effects of both the quadratic bottom drag parameterization and the topography. When the topography is variable in space, the time-stepping is performed using an auxiliary variable method due to Eskilsson & Sherwin (2005). For the simple domains used in the present study, the elliptic problem solved at each time-step is easily handled using the generalized minimal residual method (GMRES) iterative solver, and FFT, both standard in Matlab.

Full details of the numerical solution procedure of the model Equations (1)–(3) are presented in Steinmoeller *et al.* (2012b), including the numerical linear algebra and examples of analytical validation. Additionally, a grid convergence study was carried out to validate the model in the nonlinear regime using a test-case involving the emergence of solitary waves by wave propagation over a ridge. The model was also shown to be useful in a practical simulation of resonant wave generation by flow over topography. The methodology has been extended to the case of annular domains and applied to the study of mid-sized lakes that are strongly affected by both rotation and stratification in Steinmoeller *et al.* (2012a) by using a Chebyshev

pseudospectral discretization in the radial direction and a Fourier method in the annular direction.

METHODS

We consider a weakly non-hydrostatic, weakly nonlinear model of a single-layer lake. A variety of such models is available in the literature, and we base our work on the work of de la Fuente *et al*. (2008). In a one layer configuration, these models are a generalization of the well-known shallow water equations (Kundu & Cohen 2008). The shallow water equations assume that fluid motion occurs in columns, and thus formally make the assumption that vertical scales are much smaller than horizontal scales. This leads to the neglect of vertical acceleration and a reduction of the vertical equation of motion to the hydrostatic relation. Thus, while these models retain the effects of nonlinearity, the shallow water equations cannot model the dispersive properties of waves, and hence shocks may form in a finite time. While a great deal of mathematical literature is dedicated to the study of numerical solutions of systems with shocks (Teukolsky *et al.* 1994), in nature nonlinearity is often balanced by dispersion, yielding wave trains and undular bores, and precluding the formation of shocks in many situations. Dispersion effects are due to departures from the hydrostatic state, and become important when horizontal scales are on the order of the total depth. Thus as available computing power increases, and lake models resolve motions on smaller and smaller scales, dispersion becomes a vital aspect of accurate physical modelling.

A more complete lake model would consider the effects of near-bottom turbulence and surface waves through parameterizations of unresolved processes (overturning, nighttime convection, flow separation over bottom bathymetry). In the interest of simplicity, we consider only a single-layer system here, hence modelling either barotropic motions or internal waves in the 'reduced gravity' approximation (Gill 1982). The results will be presented using the language of barotropic motions with the understanding that this maps directly onto the reduced gravity case. The governing equations read,

$$h_t + \nabla(h\boldsymbol{u}) = 0 \tag{1}$$

$$(hu)_t + \nabla((hu)\boldsymbol{u}) = -gh\eta_x + \left(H^2/6\right)(\nabla\cdot(h\boldsymbol{u})_t)_x + F^{yD} \tag{2}$$

$$(hv)_t + \nabla((hv)\boldsymbol{u}) = -gh\eta_y + \left(H^2/6\right)(\nabla\cdot(h\boldsymbol{u})_t)_y + F^{xD} \tag{3}$$

where $h(x,y,t) = H(x,y) + \eta\ (x,y,t)$ is the total depth of the fluid column (sometimes referred to as the layer thickness), g is the acceleration due to gravity (or reduced gravity for internal waves), H is the mean depth, η is the free surface elevation (or layer depth for multi-level simulations), and $\boldsymbol{u} = (u,v)$ represents the depth-averaged velocity vector. For the sake of simplicity, Coriolis effects are not included in the present manuscript; however, the numerical solver is capable of such a modification. Although all plots presented have been nondimensionalized, the scale of the basins being considered was on the order of 3–5 km. At these scales, the effects of the Coriolis force are dramatically outweighed by the nonlinear and dispersive effects. For the sake of compactness, partial derivatives are written as subscripts and damping terms are written as F^{xD} and F^{yD}. Damping can thus take a variety of standard forms (such as Rayleigh damping, quadratic damping, etc.). For simplicity, we ignore damping altogether for the topography modified wave train simulations.

The second-last terms in Equations (2) and (3) are the effects of a weakly non-hydrostatic correction to the standard shallow water model. Multi-layer extensions of the system (1)–(3) with similar dispersive terms have been explored by de la Fuente *et al.* (2008). Further theoretical work on weakly non-hydrostatic multi-layer models that remain well posed in the presence of background shear has been carried out in Cotter *et al.* (2010) and this remains an active area of study.

Since Fourier methods are used and the FFT is readily available, the two-dimensional spectra are easy to calculate and do not require windowing or any other similar techniques. We choose the initial conditions to be such that there is a sinusoidal perturbation of the free surface. This perturbation leads to a standing wave pattern which, in the absence of nonlinear effects and damping, would continue to oscillate and maintain a consistent spectrum. However, both the nonlinear terms and the quadratic damping lead to the excitation of higher wave numbers. For most reasonable amplitudes, the former dominates the latter and

the evolution proceeds in the following manner. First the waves begin to steepen. When the length scales associated with the wavefront become comparable to the undisturbed layer depth, dispersive effects lead to the generation of a finite amplitude wave train. This wave train propagates back and forth across the lake, with damping slowly decreasing amplitude. The process is illustrated in Figure 1. After two half-periods (left panel) the damped system (black) has a slightly smaller amplitude than the undamped system (in red, or grey in printed version). After five half-periods (right panel), it can be seen that the damping has delayed the process of wave train formation. The damped case does eventually break down into a wave train (not shown); however, the resulting waves are of lower amplitude than the undamped counterparts.

The resolution of all two-dimensional simulations is 512 by 512 points. The lake length is 3 km by 3 km, which makes the grid spacing $dx = dy \sim 5.9$ m. The undisturbed depth of the domain is 20 m, and the topography has a maximum height of 50% of the depth (10 m). The bathymetry is taken as a smoothed square with an essentially uniform shallow region separated from an essentially uniform deep region by a transition region of width approximately 100 m (the topography thus has only a moderate slope).

The initial conditions consist of a single, mode one standing wave in the x direction and constant in the y. The surface displacement has an amplitude of 2 m (i.e. 10% of the depth of the lake). In linear theory the node of the standing wave would remain at $x = 0$.

In oligotrophic lakes, the hypothesis that sediment resuspension substantially increases nutrient availability in the lake interior and thereby affects primary productivity is taken as motivation for the use of nutrient redistribution as a passive tracer. We have chosen to forgo 'standard' pick up schemes, which are quite complex and whose domain of validity is ill-defined (for example, the parameters in such schemes are typically fitted from steady flow data). Instead we implement a simpler scheme that suits our needs while remaining computationally and theoretically as simple as possible. It is well known, both experimentally (Lou *et al.* 2000) and from a modelling standpoint (Bailey & Hamilton 1997), that the rate of sediment pick up is dependent on wind stress and thus wave-induced velocities and bottom shear stress. For this reason, we choose the simplest such relationship possible, relating the sediment resuspension and hence the rate of nutrient uptake at a point to the kinetic energy of the water directly above it. For our investigations, the initial nutrient distribution is zero (i.e. a totally barren lake). The equation for nutrient distribution is:

$$\frac{DN}{Dt} = S + \mu_N \nabla^2 N \tag{4}$$

where $\frac{DN}{Dt}$ is the material derivative. The coefficient of diffusion, μ_N is kept slightly above molecular diffusion; this diffusive term is present to ensure numerical stability rather than due to any underlying physical motivation (e.g. as a model of turbulence). Nutrient is introduced into the system via the source term, S, when the kinetic energy of

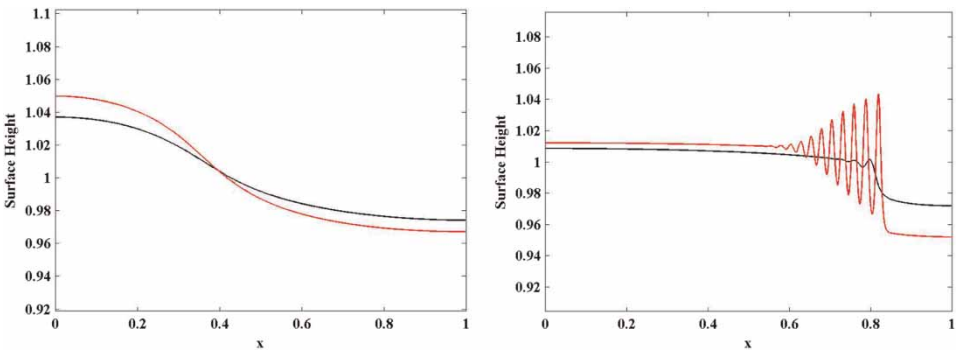

Figure 1 | Surface displacement after time 2 T (left) and 5 T (right). At early times the damped (black) and undamped (red, or grey in printed version) surface displacements are very similar. Both systems exhibit some steepening, however neither system displays any breakdown in wavefronts or wave train formation. At the later time, the undamped system (red, or grey in printed version) has steepened and formed a finite amplitude wave train while the damped system (black) has also steepened and begun the same process, but has not yet degenerated into a wave train. Please refer to the online version of this paper to see this figure in colour: http://www.iwaponline.com/wqrjc/toc.htm.

the flow exceeds a certain threshold. This threshold is chosen fairly arbitrarily based on the expected velocities induced by a certain initial perturbation. The equation for the nutrient source is:

$$S = \begin{cases} \kappa(KE - KE_{crit}) & \text{if } KE > KE_{crit} \\ 0 & \text{if } KE < KE_{crit} \end{cases} \quad (5)$$

where $KE = \frac{1}{2}\sqrt{u^2 + v^2}$, the kinetic energy, KE_{cirt} is some arbitrary threshold and κ is a constant which represents the rate of nutrient removal. In our simulations, we have used a value of $KE_{crit} = 2(m^2/s^2)$ based roughly on the maximum velocities attained in the flat system and $\kappa = 1(kgs/m^2)$.

Choosing a lower threshold creates a background influx of nutrients, which would have proven distracting. Choosing a higher threshold eliminates any resuspension. As such the value we used was chosen by trial and error to fit our initial set up so that it causes nutrient resuspension in the regions of interest (namely around the topography), but does not cause too much resuspension elsewhere, i.e. as a marker for regions of velocity which are not attained in the flat bottom case.

RESULTS

We begin by examining the effects of a region of high bottom drag on the behaviour of a seiche in a flat-bottomed lake in two dimensions. We allow the drag coefficient to vary in the north–south direction while being held uniform in the east–west direction. This allows us to examine the effects of a varying drag coefficient on the shape of the developing wavefront. The specific shape of the coefficient we have employed is a single period of a cosine. Thus the drag varies from low values near the north–south boundaries (which are periodic) to a maximum value near the centre at $y = 0$. This choice is consistent with our philosophy of the simplest model possible and facilitates analysis of the two-dimensional spectrum without any need for windowing.

All reported figures have been nondimensionalized where possible both spatially (with respect to total basin size), as well as for individual variables being considered, such as layer thickness (with respect to undisturbed depth) and fluid velocities (with respect to wave speed).

Investigations consisted of two experiments. The first experiment used values of c_D varying from the standard value (0.0025) at the north–south boundaries to three times the standard value near the centre. This pattern maintains the symmetry required for Fourier methods, and the gradual gradient demonstrates that it is the change in damping parameter that produces the largest effect on the wavefront. The second experiment had the same shape as the first, but varied from 0 at the north–south boundary to four times the standard value at the centre. While there were differences between the two experiments, the overall general features were present in both, thus we will focus only on the high-gradient case here, since the results are most easily visible and most dramatic.

We begin by considering the simulation at early times. Since the system is initialized with a standing wave, we expect the initially induced velocities to be the highest, and thus the initial wavefront deformation to be the most dramatic. At time 0.7 T (Figure 2), we can clearly observe

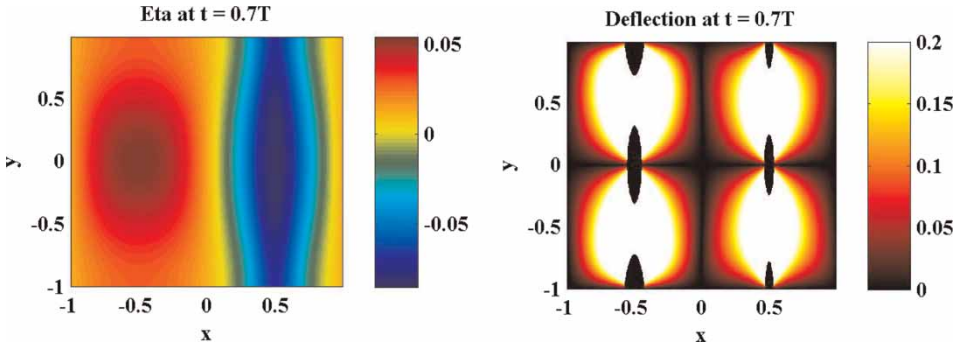

Figure 2 | Surface displacement (left) and deflection (right), the ratio of north–south velocity to total speed, of the high bottom damping coefficient case at time 0.7 T. Even at early times we observe considerable deflection of the wavefront and the regions of high deflection can be clearly identified as corresponding to the highest gradient portions of the bottom drag coefficient.

that the wavefront is deformed about the region of high damping as expected.

An important feature to consider is how much longitudinal (north–south) flow is induced by the presence of a gradient in the damping parameter and how the flow depends on the gradient. To do this, we will examine the deflection of the flow, or the ratio of the north–south velocity to the total speed of the fluid. We will use this same analysis in subsequent experiments on sediment resuspension and redistribution to examine the effects of topography on the flow. When performing this analysis, it is important to consider only areas of the fluid with a speed above some critical threshold. This cutoff is necessary to ensure that we do not have any divide by zero errors, and because (fundamentally) we are only concerned with waves of some moderate energy which are most likely to impact the lake system in a meaningful way. These interactions could include nutrient resuspension and redistribution, porous media interaction (sediment-layer interaction) or other effects on the benthos.

The actual amount of deflection of the wavefront observed after one period is fairly small. North–south deflection is systematically higher in the regions where the gradient of the damping coefficient is higher, and thus there is a clear connection between the gradient of c_D and the rate of deflection. This deflection continues to be manifested well past the point that the original seiche has broken down into wave trains (Figure 3) and again is most evident where the gradient of the bottom damping coefficient is strongest.

Another way to demonstrate this phenomenon is to consider the Fourier spectrum of the surface displacement. The initial conditions (a single cosine in the east–west direction) have no north–south component, and so any north–south variations in the spectrum must be caused by the north–south gradient in c_D. The spectrum is shown at 0.7 T and at 5 T in Figure 4. The initial conditions are shown as

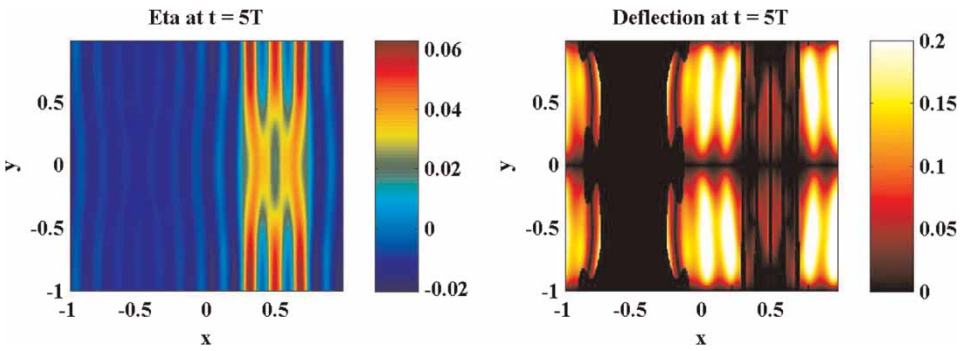

Figure 3 | Surface displacement (left) and deflection (right) of the high bottom damping coefficient case at time 5 T. The change in the wavefront is even more pronounced than before, and the deflection reflects this quite well.

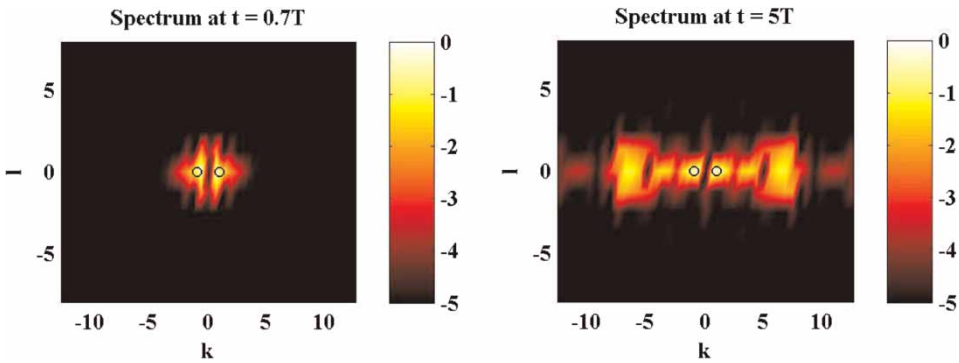

Figure 4 | Spectrum of surface displacement at 0.7 T (left) and 5 T (right) of the high gradient case. There is significantly more spectral cascade in the east–west direction (*k* direction) as is expected.

black circles (on the x axis, near the origin) in the plots of the power spectrum. Note that the spectrum disperses rapidly in both the east–west and north–south (k and l respectively) directions. It is quite clear that there is a much more substantial spreading of the spectrum in the east–west direction (i.e. much more energy goes to the small scales as the wave train forms). This would often be labelled a 'cascade' in analogy with the cascade in turbulence theory. The term 'cascade' is perhaps ambiguous here as no actual turbulence is present in the simulations. It is important to note that there has also been some spreading of the spectrum in the north–south direction, which implies deflection about the region of high damping and some measure of structure in the direction perpendicular to the dominant direction of wave propagation.

Consistent with the results in Figure 3, once the initial wave deflection has occurred, it is difficult to detect any subsequent wave deflection. This is probably because after the initial large wave the nonlinear effects take over and the subsequent velocities are sufficiently reduced that total deflection is not significantly altered.

Small shoal

We begin the investigation of flow over topography by considering a standing seiche breaking down over a rectangular, shallow region of relatively small areal extent, with a depth reduction of 50%. As mentioned above, the purpose is to present a process study where we wish to include the effects of topography, but not breaking over topography.

The system begins its evolution as a linear standing wave, but rapidly begins to steepen. Velocities over the shallow region are increased, while wave speeds decrease, with a resulting bending of the wavefront. By 6 T (Figure 5) we can observe that the surface wave has degenerated completely into a nonlinear, dispersive wave train. Namely the nonlinear aspects of the dispersive shallow water equations have done their job and the wave has steepened and broken down as in the simple, one-dimensional case discussed in the Methods section. Of more interest, however, is the deflection of this same wave. If we consider the deflection as before (right panel in Figure 5), we can see that we have a great deal of deflection at the points of steepest topographic slope (especially the corners). Since the wavefront at this time is found away from the shallow region, not much deflection is evident around the topography, as expected.

Large shoal

We now consider flow over a smoothed square with a large area of shallow depths (one half of the maximum depth). The addition of nutrients (a passive tracer in our simulations) to the system will allow us to examine the past behaviour of the wave, as well as the regions flagged as high velocity and thus of most interest. The initial tracer concentration is zero, thus all nutrient in the system must be resuspended due to wave velocities.

From Figure 6 we can see significant deflection of the surface height at early times (indeed much greater in this case when compared with the small shoal case).

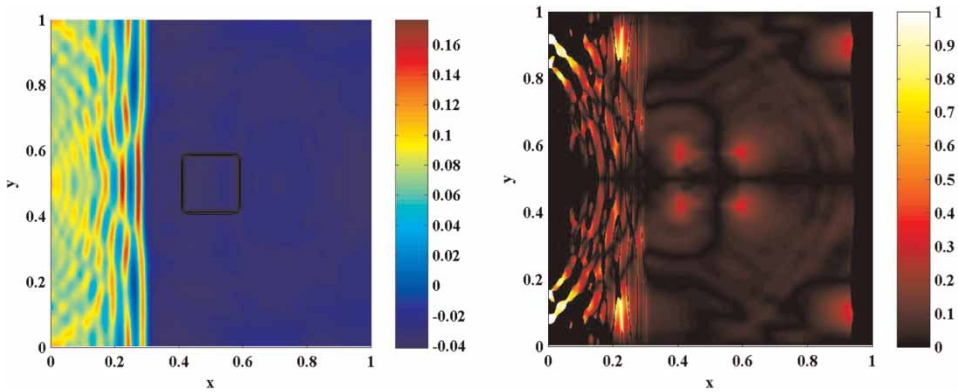

Figure 5 | Surface displacement (left) and deflection (right) of the small shoal case at time 6 T. The breakdown of the initial seiche into a wave train is clearly visible, as is the deflection about the region of shallow topography in the centre.

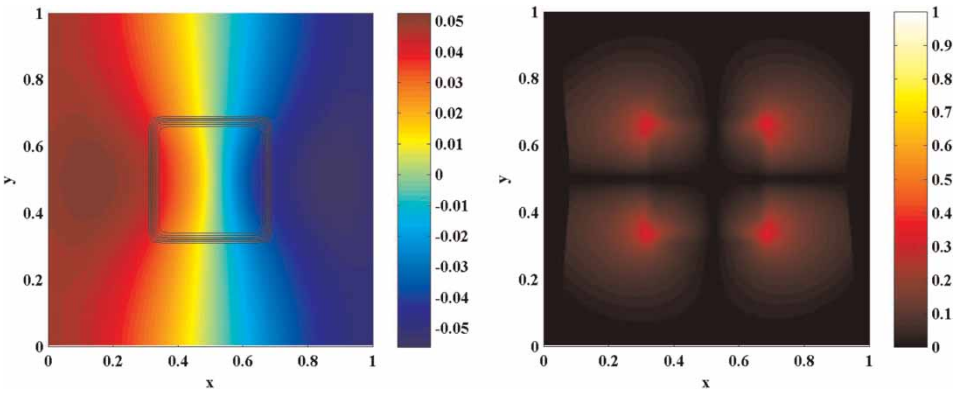

Figure 6 | Surface displacement (left) and deflection (right) of the large shoal case at time 0.7 T. Even this early in the simulation there is significant deflection over the topography and the shape of the wavefront has been altered by the presence of the shallow region.

Interestingly, there is very little difference in the deflection of the node. The velocities again are consistently higher over the topography, and again despite the larger topography, the speed does not exceed the threshold until approximately the same time as the small square case.

The nutrient resuspension at this time is almost negligible (not shown), since the initial velocities have not yet increased enough, and indeed this was the case for the small square case. Specifically, we do not find dramatically more resuspension compared with the small square case, as we might have expected if the resuspension was related strictly to the surface area of the shallow region.

Letting this system evolve in time, we can see similar behaviour to that shown in Figure 4 for the small square case. Figure 7 shows the surface height and deflection at 6 T. Regions of focusing can be seen in red in the left panel, while large, north–south velocities are evident as bright regions in the right panel. Note that some of these occur in unexpected places, and this can have implications for nutrient resuspension and transport. A similar story can be seen in the right panel of Figure 7, which shows the deflection. In particular, the deflection is maximal at the points of steepest topographic slope, and not as much over or around topography, as expected.

The deflection seen here is significant near the edges of the topography, which begs the question of whether the orientation of the topography plays a role in the deflection of the wavefront, or whether it is the reduced wave speeds over the shallow regions that are responsible. To answer this, we will consider deflection about rotated topography, below.

From Figure 8 we see that by 6 T, there has been significant nutrient resuspension and distribution throughout the

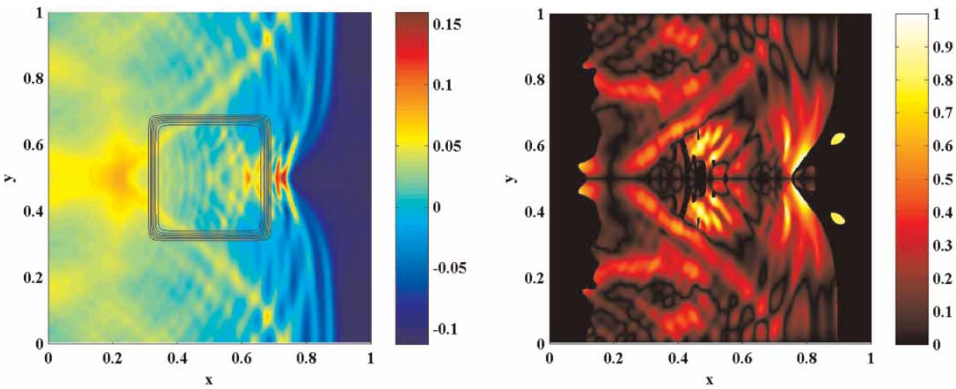

Figure 7 | Surface displacement (left) and deflection (right) of the large shoal case at time 6 T. Notice that the change in the wavefront is quite extreme near the centre of the domain. The deflection plot demonstrates that the most dramatic deflection occurs near the leading edge of the wavefront and over the shallow domain. Please refer to the online version of this paper to see this figure in colour: http://www.iwaponline.com/wqrjc/toc.htm.

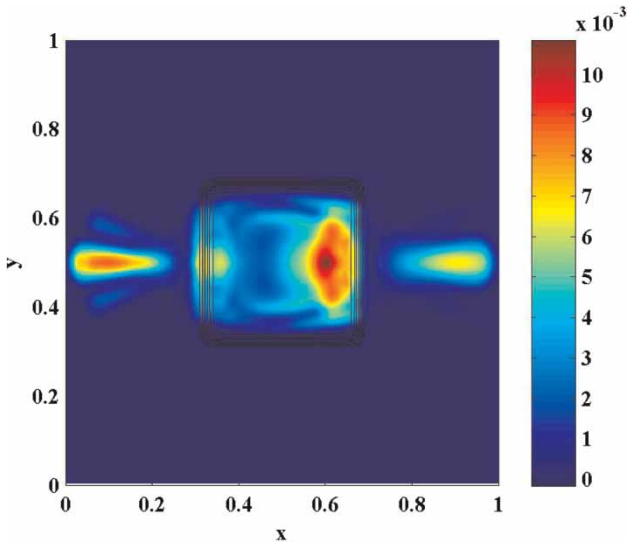

Figure 8 | Nutrient distribution at time 6 T. Clearly visible here is the fact that nutrient is generated over the topography and is then advected by the long wave in the shallow region. The regions of generation over the topography are strongest near the edges of the shallow region. Also visible here are the effects of deflection of the wave, as the advected nutrient has been significantly displaced in the north–south direction.

domain. The key point is that nutrient is introduced by the modelled sediment resuspension over the topography. This occurs almost immediately due to the increased currents in the shallow regions, associated with the long, standing waves. Subsequently, however, the nutrient is advected throughout the shallow region by the same long waves, and eventually by the developing wave trains. The wave trains themselves are modified by the topography, as seen in the deflection plot in Figure 7. This finally results in the interesting patterns we observe in Figure 8, where the nutrient blob has been advected in the x direction and dispersed in the y direction through the shallows. The teardrop patterns are created by the wave train as it steepens and reflects off the wall. It is particularly interesting that it is the initial long wave, and not the subsequent wave train which is responsible for most of the resuspension and transport of nutrient in the shallow region. The wave trains are responsible for some of the more complex aspects of the nutrient spatial distribution, as seen in Figure 8, as well as the eventual pick up near the walls, visible in Figures 8 and 9 when the steepening of the nonlinear waves triggers the resuspension scheme.

As the most common application of numerical models is to compare with point measurements, we seek here to generate artificial experimental data to emulate what a measuring station would observe. The goal is to provide another means of demonstrating the cascade from basin-scale to high frequency effects. We consider three points throughout the domain and around the topography. Figure 9 shows the placement of the 'data sites' where we will consider kinetic energy and nutrient distributions. While we expect our data to exhibit variation on many time-scales, we do not expect it to be as 'noisy' as real world data would be. This is partly because our artificial data do not have measurement error associated with it, and our model has no parameterizations (for mixing, for example) or stochastic elements (for wind forcing, for example). Thus any observed variations in the measurements must come from the basin-scale seiche breaking down into high frequency wave trains. Also note that unlike the Lake Kinneret measurements of Hodges *et al.* (2000) and Boegman *et al.* (2003) we have a system with no energy input.

The measurements reveal that as expected there is a trend toward short, high frequency waves.

The data point in the shallow region over the topography shows the most activity. The kinetic energy (and thus velocities) reach the critical threshold (scaled $KE = 1$), and thus nutrient is resuspended and subsequently advected throughout the shallows and some way into the deeper regions. In contrast, the region just outside the shallows, directly south of the previous field point, exhibits virtually identical temporal characteristics of the kinetic energy profile; however the flow at this point never triggers the resuspension scheme.

The data point in the deep region, well away from the shallows and near the lake boundary, shows that the nutrient levels there are triggered by discrete events, and only for late times. This implies that it is only when the non-hydrostatic wave train is formed, passes through and reflects off the lake boundary, that resuspension takes place. From the kinetic energy profile it is also clear that at the chosen location and at one of the 'measured' times the resuspension threshold is never reached.

This suggests that model integrations, with their lake-wide data coverage, allow for the identification of sites more likely to exhibit sediment resuspension. Moreover, it presents a unique aspect of the problem of measurement, namely that in order to capture the basin-scale resuspension

behaviour, a large quantity of measurement sites is required. Additionally it is very difficult to analytically show the deflection of the wavefront from sparse measurements. In contrast, the kinetic energy snapshots (as is visible in the kinetic energy snapshot in Figure 9) clearly demonstrate this effect.

Rotated topography

Now we examine a topography identical to the large square in area, but rotated 45 degrees, so that the leading edge of the wave first reaches the corner of the topography. This set up of topography is also symmetric about $y = 0.5$, although as we shall see, there are significant differences that arise from orientation. This is done to consider whether the deflection caused by the presence of topography can be significantly altered by the orientation of the seiche with respect to the topography. Note however that the average depth of the domain is unchanged from the large square case.

At early times (Figure 10) we can see that, while the surface shape and the deflection are both slightly different from the large square case, the differences are not dramatic. In particular, we can see that the node deflection is quite similar to the large square case.

At later times (Figure 11, comparing with Figure 7) we can see that the regions of wave focusing (the yellows and reds in the left panel) have a slightly different location. It is the north–south deflections (right panel), however, that have the largest differences. This different pattern of north–south currents (and waveforms in general) subsequently manifests itself in the pick up and transport of nutrient.

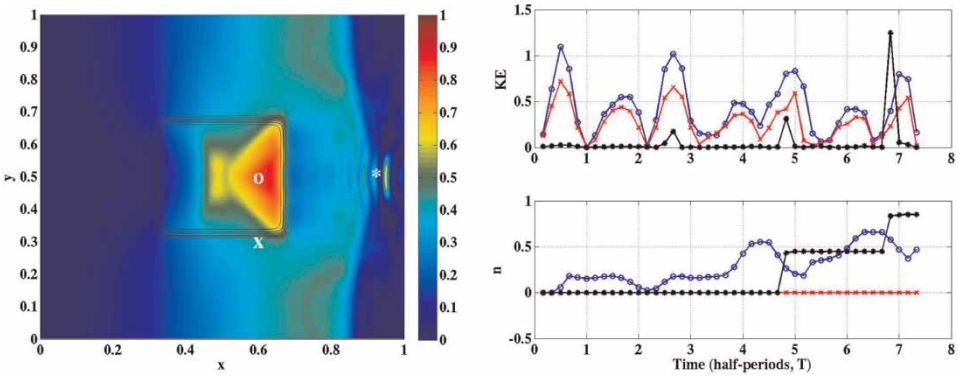

Figure 9 | Kinetic energy at 4.85 T and location of field sites used for artificial data creation (left); and kinetic energy and nutrient measurements at said sites for the length of the simulation output at intervals of T/6 (right). The kinetic energy and nutrients have been scaled by the critical pick up threshold and maximum nutrient levels, respectively.

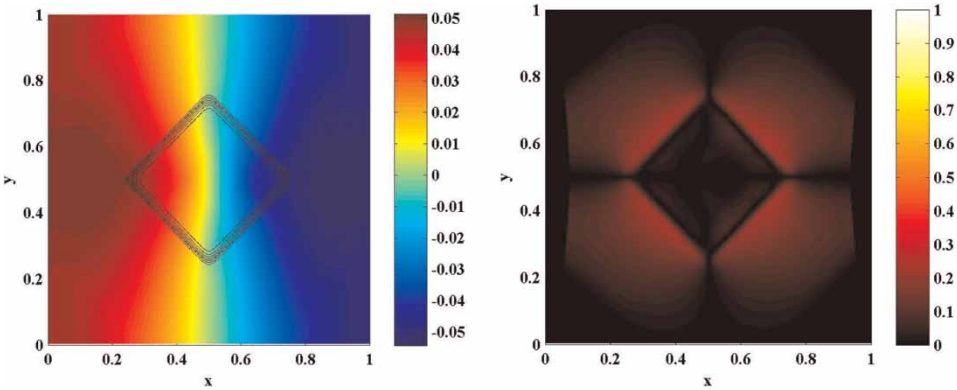

Figure 10 | Surface displacement (left) and deflection (right) of the rotated topography case at time 0.7 T. Again we see some deflection in the shape of the wave; however in this case there is significantly less deflection over the topography itself compared with the large square case.

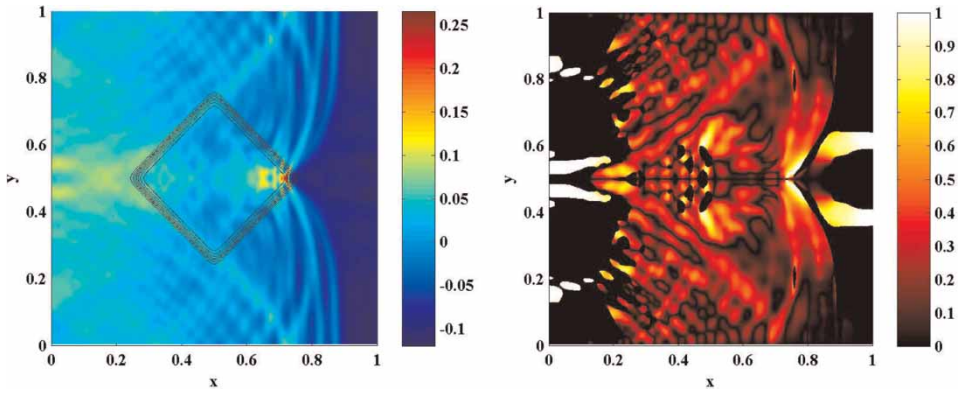

Figure 11 | Surface displacement (left) and deflection (right) of the rotated topography case at time 6 T. Once again the deviation in the shape of the wavefront is very dramatic, but now the regions of highest deflection are outside the shallow region. Please refer to the online version of this paper to see this figure in colour: http://www.iwaponline.com/wqrjc/toc.htm.

While there are some small differences in the kinetic energy profile of the rotated case and the large square (not shown), the overall structure is also very similar. The key difference between the two is that the regions of high kinetic energy, and thus highest nutrient resuspension, occur not near the centre of the topography, but at the north and south edges.

If we consider the nutrient distribution at time 6 T (Figure 12), we see that the regions of nutrient generation have effectively flagged regions of high velocity. Additionally this distribution demonstrates the flow's ability to advect resuspended nutrient. Interestingly, we do not observe the dramatic deflection about topography that we expected. Rather we see significant pick up along the line $y = 0.5$, as well as near the north–south edges of the domain.

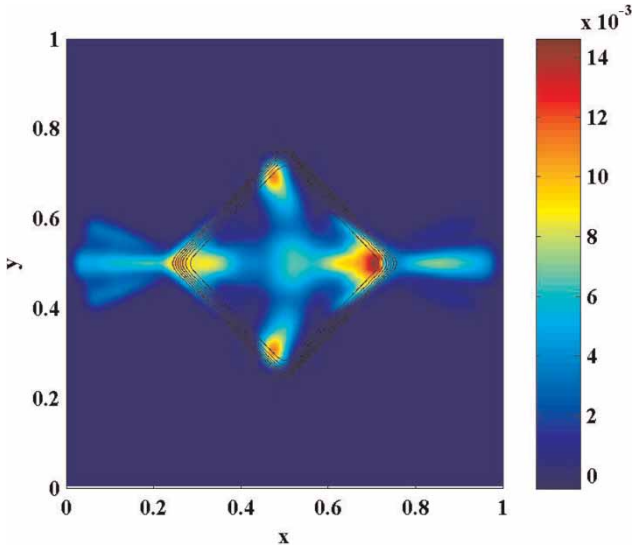

Figure 12 | Nutrient distribution at time 6 T. Visible again are the regions of wave generation near the corners of the topography as well as the effects of long-wave advection whereby nutrient is generated over the topography and then advected east–west and dispersed north–south.

DISCUSSION

We have seen that the evolution of the nonlinear aspects of wave propagation is altered by the presence of quadratic bottom drag. However, it is also quite clear from the one-dimensional simulations that the majority of steepening and spectral cascade is due to the nonlinearity of the shallow water equations, rather than the presence of nonlinear damping.

For high speeds, the quadratic damping is an extremely efficient means of removing energy from the system and hence preventing significant wave steepening. However, quadratic damping is also quite sensitive to the choice of damping parameter, C_D, and for low speeds damping is in fact weak, or even nearly absent. A small damping parameter, such as we have investigated herein does not have the dramatic damping effect that we might expect *a priori*. Experiments that varied the magnitude of a spatially constant C_D (not shown) suggest that the damping of the emerging wave train is gradual. At 10 times the value of C_D used herein, the wave train is weak, but still discernible while at 20 times the value used herein the wave train is

essentially imperceptible. However, it is our belief that this represents an unrealistic damping parameter, and so we did not explore this scenario in detail here.

In our two-dimensional simulations we discovered that there is a natural tendency in the flow to divert around the regions of highest damping. In this way, regions of high friction tend to influence the flow in a similar manner to bathymetry, diverting flow and inducing a bending of the developing in wave trains from a direction aligned with the winds that forced them.

In the section concerning the impact of bathymetry on flow characteristics, we saw, as predicted, that topography has a significant effect upon both the dynamics of the flow and on the subsequent nutrient distribution. Having chosen an *a priori* threshold velocity which is just barely triggered by the flat-bottom case, we can clearly see the areas that are most influenced by the addition of topography. Bathymetric hills and valleys can thus have a profound influence on the lake ecosystem. Indeed the presence of even the geometrically simple topographical features presented herein dramatically alters the dynamics of the system as well as the nutrient distribution and dispersal.

The nonlinear and non-hydrostatic nature of the model is quite clearly visible in the degeneration of the original seiche into a wave train. Note however that while we have observed how the wave train can modify the nutrient distribution in the lake, it is the initial long waves that are responsible for the bulk of nutrient resuspension in the shallow regions. We found that in the shallows the long waves are responsible for the bulk of the sediment resuspension, with the eventual wave trains only playing a secondary role. In the deep regions it is the nonlinear, non-hydrostatic wave trains that were the only cause of resuspension. In future work the present simulations will be contrasted with process studies of internal wave phenomena that can lead to more sediment resuspension than the above-mentioned long waves. Some evidence for such phenomena exists from numerical simulations and experiments in continuously stratified fluids (Carr *et al.* 2010).

A more significant step forward would be to consider basin-scale seiche effects using continuously stratified models, possibly bridging the gap between basin scales and the bottom boundary layer. This should be possible for small lakes in a two-dimensional configuration. From a more physical standpoint, another interesting extension would be the addition of a non-Newtonian or porous model of the bottom layer (see for example, Nield & Joseph (1985) and Hearn *et al.* (2001)).

The idealized model presented above is a useful tool in helping to understand the interaction between basin-scale seiches, bottom topography and drag. The goal is to provide fundamental insight into the nature of these interactions using high-order numerics and a systematic approach to individual effects. While not directly related to any particular set of lake measurements, models like the one above provide a guide to which portions of parameter space yield novel physical phenomena. These phenomena can subsequently be explored by more complete (and numerically much more costly) models. It is worth noting that parameter fitting to single-point measurements, which is commonly carried out as a model 'calibration' exercise, has been criticized in a variety of disciplines as not leading to any substantial improvement in model robustness. Carter *et al.* (2006) discuss the difficulties of calibrated models in finance modelling, Seibert & McDonnell (2002) discuss uncertainty in catchment hydrology, and Beven (1993) makes a comprehensive assessment of the dangers of calibrated models as predictive tools in hydrological models. Moreover, for an essentially inviscid model such as the one used in the above there is little to 'calibrate' and the qualitative results are in good agreement with what we expect to see and what can be measured in the real world.

ACKNOWLEDGEMENTS

This work was supported by the Natural Sciences and Engineering Research Council of Canada.

REFERENCES

Arbic, B. K. & Scott, R. B. 2008 On quadratic bottom drag, geostrophic turbulence, and oceanic mesoscale eddies. *J. Phys. Oceanogr.* **38**, 84.

Bailey, M. C. & Hamilton, D. P. 1997 Wind induced sediment resuspension: a lake-wide model. *Ecol. Model.* **99**, 217–228.

Beven, K. 1993 Prophecy, reality and uncertainty in distributed hydrological modelling. *Adv. Water Resour.* **16**, 41–51.

Boegman, L., Imberger, J., Ivey, G. N. & Antenucci, J. P. 2003 High-frequency internal waves in large stratified lakes. *Limnol. Oceanogr.* **48**, 895–919.

Bowers, D. G., Rippeth, T. P. & Simpson, J. H. 1991 Tidal friction in a sea with two equal semidiurnal tidal constituents. *Cont. Shelf Res.* **11**, 203–209.

Boyd, J. P. 2001 *Chebyshev and Fourier Spectral Methods*. Dover, New York.

Carr, M., Stastna, M. & Davies, P. A. 2010 Internal solitary wave-induced flow over a corrugated bed. *Ocean Dyn.* **4**, 1007–1025.

Carter, J. N., Ballester, P. J., Tavassoli, Z. & King, P. R. 2006 Our calibrated model has poor predictive value: an example from the petroleum industry. *Reliab. Eng. Syst. Saf.* **91**, 1373–1381.

Cotter, C. J., Holm, D. D. & Percival, J. R. 2010 The square root depth wave equations. *Proc. R. Soc. A*, **456**, 3621–3633.

de la Fuente, A., Shimizu, K., Imberger, J. & Nino, Y. 2008 The evolution of internal waves in a rotating, stratified, circular basin and the influence of weakly nonlinear and non-hydrostatic accelerations. *Limnol. Oceanogr.* **53**, 2738–2748.

Durran, D. R. 1991 The third-order Adams-Bashforth method: an attractive alternative to leapfrog time differencing. *Monthly Weather Rev.* **119.3**, 702–720.

Eskilsson, C. & Sherwin, S. 2005 Spectral discontinuous Galerkin methods for modeling 2D Bounssinesq equations. *J. Sci. Comp.* **22**, 269–288.

Feddersen, F., Gallagher, E. L., Guza, R. T. & Elgar, S. 2003 The drag coefficient, bottom roughness, and wave-breaking in the nearshore. *Coast. Eng.* **48**, 189–195.

Fernando, H. J. S., Samarawickrama, S. P., Balasubramanian, S., Hettiarachchi, S. S. L. & Voropayev, S. 2008 Effects of porous barriers such as coral reefs on coastal wave propagation. *J. Hydro-Environ. Res.* **1**, 187–194.

Fischer, H., List, E., Koh, R., Imberger, J. & Brooks, N. 1979 *Mixing in Inland and Coastal Waters*. Academic Press, New York.

Fredsoe, J. & Deigaard, R. 1992 *Mechanics of Coastal Sediment Transport*. World Scientific, River Edge, NJ.

Gill, A. E. 1982 *Atmosphere-Ocean Dynamics*. Academic Press, London.

Godin, G. & Martnez, A. 1994 Numerical experiments to investigate the effects of quadratic friction on the propagation of tides in a channel. *Cont. Shelf Res.* **14**, 723–748.

Hasselmann, D. E., Dunckel, M. & Ewing, J. A. 1980 Directional wave spectra observed during JONSWAP 1973. *J. Phys. Oceanogr.* **10.8**, 1264–1280.

Hearn, C., Atkinson, M. & Falter, J. 2001 A physical derivation of nutrient-uptake rates in coral reefs: effects of roughness and waves. *Coral Reefs* **20**, 347–356.

Hodges, B. R., Imberger, J., Saggio, J. & Winters, K. B. 2000 Modeling basin-scale internal waves in a stratified lake. *Limnol. Oceanogr.* **45**, 1603–1620.

Imberger, J. 1998 *Physical Processes in Lakes and Oceans*. American Geophysical Union, Washington, DC.

Koblinsky, C. 1981 The M2 tide on the West Florida Shelf. *Deep Sea Res. Part I: Oceanogr. Res.* **28**, 1517–1532.

Kundu, P. K. & Cohen, I. M. 2008 *Fluid Mechanics*. Elsevier, Oxford.

Kunkel, C. M., Hallberg, R. W. & Oppenheimer, M. 2006 Coral reefs reduce tsunami impact in model simulations. *Geophys. Res. Lett.* **332**, L23612.

Longuet-Higgins, M. S. 1970 Longshore currents generated by obliquely incident sea waves, 2. *J. Geophys. Res.* **75**, 6790–6801.

Lou, J., Schwab, D. J., Beletsky, D. & Hawley, N. 2000 A model of sediment resuspension and transport dynamics in southern Lake Michigan. *J. Geophys. Res.* **105**, 6591–6610.

Marshall, J., Adcroft, A., Campin, J. M., Dutkiewicz, S., Evangelinos, C., Ferreira, D., Forget, G., Fox-Kemper, B., Heimbach, P., Hill, C., Hill, E., Hill, H., Jahn, O., Losch, M., Maze, G., Menemenlis, D. & Molod, A. 2012 *MITgcm User Manual*. MIT EAPS, Cambridge, MA.

Nield, D. A. & Joseph, D. D. 1985 Effects of quadratic drag on convection in a saturated porous medium. *Phys. Fluids* **28**, 995–997.

Ozkan-Haller, H. T. & Kirby, J. T. 1999 Nonlinear evolution of shear instabilities of the longshore current: a comparison of observations and computations. *J. Geophys. Res.-Oceans* **104**, 25953–25984.

Pingree, R. 1983 Spring tides and quadratic friction. *Deep Sea Res. Part I: Oceanogr. Res.* **30**, 929–944.

Seibert, J. & McDonnell, J. J. 2002 On the dialog between experimentalist and modeler in catchment hydrology: use of soft data for multicriteria model calibration. *Water Resour. Res.* **38**, 1241.

Steinmoeller, D. T., Stastna, M. & Lamb, K. G. 2012a Pseudospectral methods for Boussinesq-type equations in an annular domain with applications to mid-sized lakes. *J. Comput. Sci.* (Epub ahead of print.)

Steinmoeller, D. T., Stastna, M. & Lamb, K. G. 2012b Fourier pseudospectral methods for 2D Boussinesq-type equations. *Ocean Model.* **52–53**, 76–89.

Teukolsky, S. A., Vetterling, W. T. & Flannery, B. P. 1994 *Numerical Recipes*. Cambridge University Press, New York.

Timmerman, P. & van der Weele, J. P. 1999 On the rise and fall of a ball with linear or quadratic drag. *Am. J. Phys.* **67**, 538–546.

Ullman, D. S. & Wilson, R. E. 1998 Model parameter estimation from data assimilation modeling: temporal and spatial variability of the bottom drag coefficient. *J. Geophys. Res.-Oceans* **103**, 5531–5549.

Van Rijn, L. C. 1994 *Principles of Sediment Transport in Rivers, Estuaries, and Coastal Seas*. Aqua Publications, Netherlands.

Wuest, A. & Lorke, A. 2003 Small-scale hydrodynamics in lakes. *Ann. Rev. Fluid Mech.* **35**, 373–412.

First received 18 January 2012; accepted in revised form 10 October 2012